A user programmed cohesive zone finite element for ANSYS Mechanical

Lindgaard, E.; Bak, B. L.V.; Glud, J. A.; Sjølund, J.; Christensen, E. T.

Published in:
Engineering Fracture Mechanics

DOI (link to publication from Publisher):
10.1016/j.engfracmech.2017.05.026

Publication date:
2017

Document Version
Accepted author manuscript, peer reviewed version

A User Programmed Cohesive Zone Finite Element for ANSYS Mechanical

E. Lindgaard[a,*], B.L.V. Bak[a], J.A. Glud[a], J. Sjølund[a], E.T. Christensen[a]

[a]*Department of Materials and Production, Aalborg University, Fibigerstræde 16, Aalborg DK-9220, Denmark*

Abstract

A cohesive finite element implemented as a user programmable feature (UPF) in ANSYS Mechanical is presented. Non-standard post-processing capabilities compared to current available cohesive elements in commercial finite element software packages have been defined and implemented. A description of the element formulation and the post-processing options are provided. Simulation studies are presented which serves to verify the implementation and compare the performance to ANSYS INTER205 cohesive element. The results show that the implemented element performs better in terms of ability to converge to a solution and requires fewer iterations to converge in the incremental Newton-Raphson solution procedure used. Additionally, a sensitivity study about the typical remedy to obtain convergent solutions having coarse meshes by lowering the onset traction is conducted. The study brings new insight to the effect of lowering the onset traction and recommendations of practical usage in case of coarse meshes are outlined.

Keywords: Delamination, Cohesive zone models, Benchmark study, User defined finite element

1. Introduction

One of the common failure types of laminated long fibrous composite materials is delamination. Delaminations can be regarded as cracks and are in many situations limited to propagate in the interface between the laminae. As a consequence the potential crack extension path is known and the crack loading mode is often a combination of the three basic modes I, II, and III. The topic of modelling and simulation of delamination propagation is vast and have been treated both in a classical linear elastic fracture mechanical framework and a cohesive zone model (CZM) framework. In order to limit the extent of the introduction only the main works leading to the state-of-the-art cohesive zone model finite elements for 3D finite element models are presented here. The theory and models regarding crack propagation were founded with the energy approach by [1] where an energy criterion for crack propagation was formulated. Based on linear elastic solutions for displacements and stresses around a crack tip, [2] reformulated the crack growth criterion to a stress based criterion via stress intensity factors which describes the intensity of the stress singularity at the crack tip. [3] addressed the problems related to the interpretation of the stress singularity by formulating a cohesive model, where tractions on the crack faces close to the crack tip leads to finite stresses at the crack tip. At the same time [4] worked on cracks in steel sheets with yielding and formulated a mathematically equivalent model with finite stress at the crack tip but with a different perspective on the physics leading to this result. In the theory of cohesive zone models, crack propagation can be viewed as a matter of overcoming the cohesive forces, described by a traction-separation law, holding together the material. Hillerborg et al. [5] extended a cohesive zone model with the assumption that the maximum traction of the cohesive law can be used as a strength criterion for the formation of new cracks. Later Needleman [6] used a CZM in a 2D finite element analysis of interface cracks and modelled the entire interface, not just the cohesive zone, with its own constitutive relation between tractions and displacements (the cohesive law). The combination of the approaches of Hillerborg et al. and Needleman enables a very automated analysis without the need to change the geometry or mesh during crack formation and propagation.

☆Postprint version, final version available at https://doi.org/10.1016/j.engfracmech.2017.05.026

*Correspondence to: Department of Materials and Production, Aalborg University (AAU), Fibigerstræde 16, 9220 Aalborg East, Denmark. Corresponding author E-mail address: elo@m-tech.aau.dk

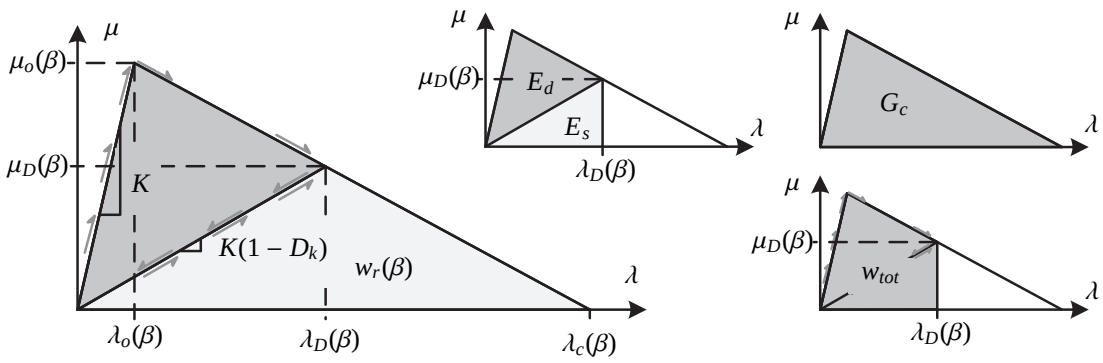

Figure 1: Equivalent one dimensional cohesive law for mixed mode quasi-static delamination propagation simulation. Note that the cohesive law is shown for a constant mode mixity β [15, 18].

The finite element implementation of the CZM has been further developed for 3D fracture analysis in [7–15]. The element formulation used here is based on [15, 16]

The cohesive zone element described here is implemented in ANSYS Mechanical [17] as a user programmable feature (UPF)[1]. The cohesive zone element is implemented as an UPF in ANSYS Mechanical for several reasons. The first reason is to establish a framework for doing research in formulating cohesive zone models and finite element formulations. The second reason is to have access to and control over the cohesive element formulation and options as these heavily influence the results and convergence behaviour of the finite element model. The third reason is that by implementing the cohesive element in a commercial FE code it is possible to do benchmarks of the different element formulations using commercially available solvers as well as facilitate easier collaboration with research partners. Finally, implementing a cohesive zone element in ANSYS enables the possibility of defining non-standard element result output. For the readily available cohesive zone elements in ANSYS it is only possible to read out and plot the openings and tractions of the element in a more or less randomly defined local coordinate system defined by the node numbering of the element.

The manuscript is organized as follows. Firstly, the cohesive element is described in Sec. 2. Then studies that verify the implementation of the element and demonstrate the performance of the element are presented in Sec. 3. This is followed by a study in Sec. 4 on the typical remedy to obtain convergent solutions in coarse meshes, which involves an artificial reduction of the onset traction of the cohesive law. Finally, conclusions are provided in Sec. 5.

2. Cohesive element

The cohesive element is based on the quasi-static damage model from [15] and the element integration scheme described in [16]. A short summary of the element formulation is presented in the following.

2.1. Kinematics and constitutive law

The traction-separation relation is formulated as an equivalent one-dimensional bilinear cohesive law, see Fig. 1. The cohesive law relates the interface separation norm λ and the equivalent one dimensional interface traction μ which are defined as:

$$\begin{aligned} &\lambda = \sqrt{(\delta_I)^2 + (\delta_s)^2} \qquad \text{where} \qquad \delta_I = \frac{1}{2}(\delta_3 + |\delta_3|) \qquad \delta_s = \sqrt{(\delta_1)^2 + (\delta_2)^2} \\ &\mu = (1 - D_k) K \lambda \end{aligned} \tag{1}$$

[1] A compiled version of the presented element implementation can be granted upon e-mail request to the authors of this paper.

where δ_I is related to mode I crack opening and δ_s is a shear separation. The shape of the cohesive law is defined by the initial stiffness K, the equivalent one dimensional onset separation λ_o, and the equivalent one dimensional critical separation λ_c which are functions of the mode mixity β:

$$\beta = \frac{\delta_s}{\delta_I + \delta_s} \tag{2}$$

The onset separation λ_o and the critical separation λ_c are defined as:

$$\lambda_o = \frac{\mu_o}{K}, \qquad \lambda_c = \frac{2G_c}{\mu_o} \tag{3}$$

The critical energy release rate G_c and equivalent single mode onset traction μ_o are in general mode dependent and are therefore determined using a modified BK-criterion [15, 19] expressed in the local opening displacement based mode mixity β.

$$\begin{aligned} G_c &= G_{Ic} + (G_{IIc} - G_{Ic})B^\eta \\ \mu_o &= \sqrt{(\tau_{Io})^2 + [(\tau_{IIo})^2 - (\tau_{Io})^2]B^\eta} \\ \text{where} \quad B &= \frac{\beta^2}{2\beta^2 - 2\beta + 1} \end{aligned} \tag{4}$$

where subscripts I and II denote the pure mode I and II values, respectively, and η is an experimentally determined mode interaction parameter. In 3D delamination problems G_{IIc} and τ_{IIo} in the modified BK-criterion are substituted with G_{sc} and τ_{so}, respectively, implicitly assuming that $G_{sc} = G_{IIc} = G_{IIIc}$ and $\tau_{so} = \tau_{IIo} = \tau_{IIIo}$.

The damage criterion for quasi-static damage in incremental form is formulated such that the current damage at any current time t_c is given as:

$$D^k = \min(\max(0, s^t), 1) \qquad \forall \ t \in [0, t_c] \quad \text{where} \tag{5}$$

$$s^t = \frac{\lambda_c^t(\lambda^t - \lambda_o^t)}{\lambda^t(\lambda_c^t - \lambda_o^t)} \tag{6}$$

Note, that the quantities λ_c and λ_o are dependent on the mode mixity β. The opening displacement norm associated with the current damage D^k and mode mixity β is defined as:

$$\lambda_D = \frac{\lambda_o \lambda_c}{\lambda_c - D^k(\lambda_c - \lambda_o)} \tag{7}$$

The stiffness degrading damage variable is not meaningful for post-processing when evaluating the damage state in the damage process zone which is defined as the area where $D^k \in]0, 1[$. Instead an energy based damage variable D^e is used which is more meaningful in this regard. The energy based damage variable D^e is defined as:

$$D^e = \frac{G_c - w_r}{G_c} \tag{8}$$

where w_r is the remaining ability to do non-conservative work per area of the interface and is given as:

$$w_r = \frac{1}{2}\lambda_D(1 - D^k)K\lambda_c \tag{9}$$

For crack propagation under constant mode mixity β the energy based damage variable D^e is proportional to the energy dissipated per area interface. However, this is not the case for a variable crack loading mode situation. In such situations the dissipated energy per area E_d is useful for post-processing:

$$E_d = \int_0^{\lambda_D} \mu d\lambda - E_s \tag{10}$$

where the stored elastic energy E_s is defined as:

$$E_s = \frac{1}{2}\mu_D \lambda_D \tag{11}$$

The average mode mixity, β_{avg}, and the average energy component mode-mixity given by the $B-$parameter in the BK-criterion, B_{avg}, are defined as:

$$\beta_{avg} = \frac{\int_0^{D^e} \beta dD^e}{D^e}, \qquad B_{avg} = \frac{\int_0^{D^e} B dD^e}{D^e} \tag{12}$$

which proves to be useful measures in order to study in which mode the dominant part of the damage process at each material point has taken place.

Both the dissipated energy per area E_d and the average mode mixities during the damage evolution, β_{avg} and B_{avg}, are evaluated numerically using a 2-point Newton-Cotes integration rule.

2.2. Element formulation

The element is an 8-noded zero thickness brick element with linear interpolation of the separation of the upper and lower surface on the middle surface where the natural coordinates ξ and η are defined, see Fig. 2. The numerical

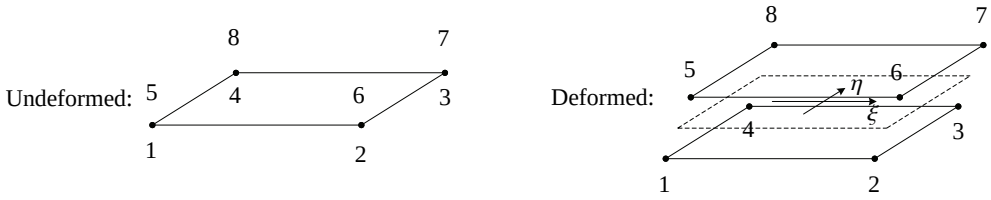

Figure 2: Cohesive element in undeformed and deformed configuration.

integration of the element internal force vector and the element tangent stiffness matrix is done according to the adaptive integration scheme described in [16] which improves the accuracy of the response and ability to converge to a solution. The adaptive integration scheme increases the number of integration points if an element is located in the damage process zone (where areas of the elements are partly damaged $D_k \in]0, 1[$). This is illustrated in Fig. 3.

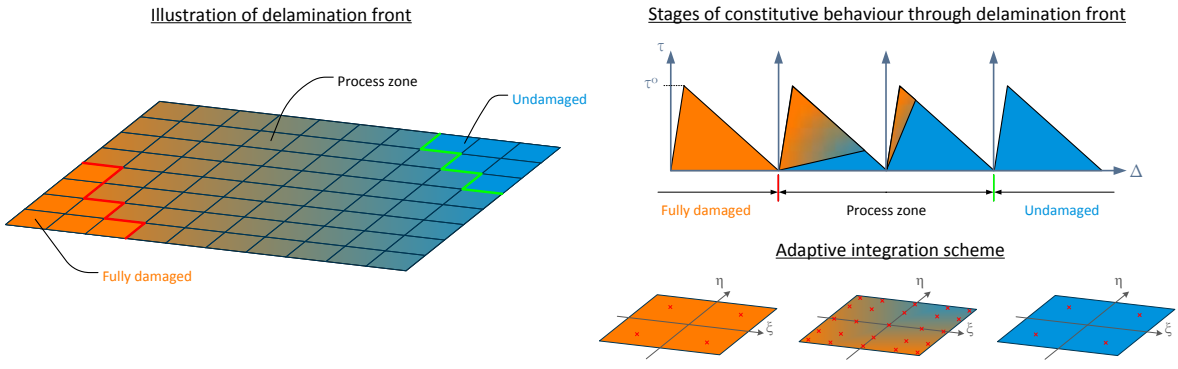

Figure 3: Illustration of the adaptive integration scheme of [16] using a Gauss-Legendre quadrature rule.

2.3. Application and post processing capabilities

The cohesive zone element is implemented in ANSYS Mechanical [17] as a user programmable feature (UPF). The finite element is coded in Fortran90 and compiled and linked with ANSYS using the Intel visual fortran compiler [20]. The element can be accessed in ANSYS using the graphical interface during pre- and post-processing of the

model. In order to create a mesh the automatic meshing feature for the element INTER205 is used as this element has the same topology. As mentioned in the introduction it is only possible to read out and plot the openings and tractions of the available cohesive zone elements in ANSYS. Furthermore, the ANSYS output is not coordinate transformed to the element coordinate system meaning that the different mode openings are output more or less randomly according to the node numbering of the individual elements. In the implementation presented here the element output has been extended over the INTER205 element to also include:

- Element tractions and openings plotted in the element coordinate system (ξ, η)
- Stiffness damage parameter D^k, cf. Eq. (5)
- Energy based damage parameter D^e, cf. Eq. (8)
- Stored elastic energy per area E_s, cf. Eq. (11)
- Dissipated energy per area E_d, cf. Eq. (10)
- Mode mixity β, cf. Eq. (2)
- Average mode mixities during the damage evolution, β_{avg} and B_{avg}, cf. Eq. (12)

The element output can be accessed through the post-processing GUI in ANSYS Mechanical to create contour plots on the deformed and undeformed mesh.

3. Element verification and performance

The following studies have been conducted in order to verify the element implementation and to quantify the performance of the element relatively to the available ANSYS INTER205 element:

- Verify that the implementation can reproduce the applied mixed mode bilinear law in simulation.
- Verification of the implementation of the kinematics and the coordinate transformations in rigid body translation and rotation simulations.
- Verification of the bookkeeping of UPF elements when using automatic cohesive meshing facilities in ANSYS.
- Verification as well as a study on the influence of the nodal force and energy dissipation of the adaptive integration scheme in single element studies.
- Comparison of the implemented element and ANSYS INTER205 in terms of the convergence rate and ability to converge.

All studies are solved as a displacement controlled static analysis using the Newton-Raphson solver unless otherwise specified.

3.1. Element implementation verification

In order to verify the element implementation several studies have been conducted on a single element model shown in Fig. 4. Here the implementation of the kinematics, the coordinate transformations, and the constitutive law of the cohesive zone element have been tested and verified. The model works in conjunction with a MATLAB [21] script, that can generate nodal displacements for the element according to prescribed rigid body rotations and rigid body translations, as shown in Fig. 4 (left). Opening displacements are always applied relative to the element orientation so that the element should always provide the same results. In this way it can be verified whether the formulation of the element kinematics has been implemented correctly. In order to also verify the implementation of the constitutive law used as input, cf. Eqs. (1–4), complete sweeps of the (δ_3,δ_s) opening displacement space (normal, shear opening), i.e. $\delta_3 \in [0, \delta_{3c}]$ and $\delta_s \in [0, \delta_{sc}]$, are made by conducting a series of analyses at certain directions in (δ_3,δ_s) opening displacement space. The used material data for the element verification test is shown in Tab. 1. For each direction in (δ_3,δ_s) opening displacement space an analysis is performed and data is recorded for each substep in the Newton-Raphson solution. Using this procedure the entire (δ_3,δ_s) opening displacement space versus the traction norm μ is simulated and collectively shown in Fig. 4 right, which within numerical roundoff errors perfectly reproduces the theoretical mixed-mode constitutive law specified as input. These tests have been conducted at several configurations of the element, i.e. at several combinations of rigid body rotations and translations.

Table 1: Cohesive interface properties used in the verification studies of the element implementation.

$G_{Ic} = 0.969$ N/mm	$G_{IIc} = 1.717$ N/mm	$\tau_{Io} = 4$ MPa	$\tau_{so} = 5$ MPa	$K = 10^6$ N/mm^3

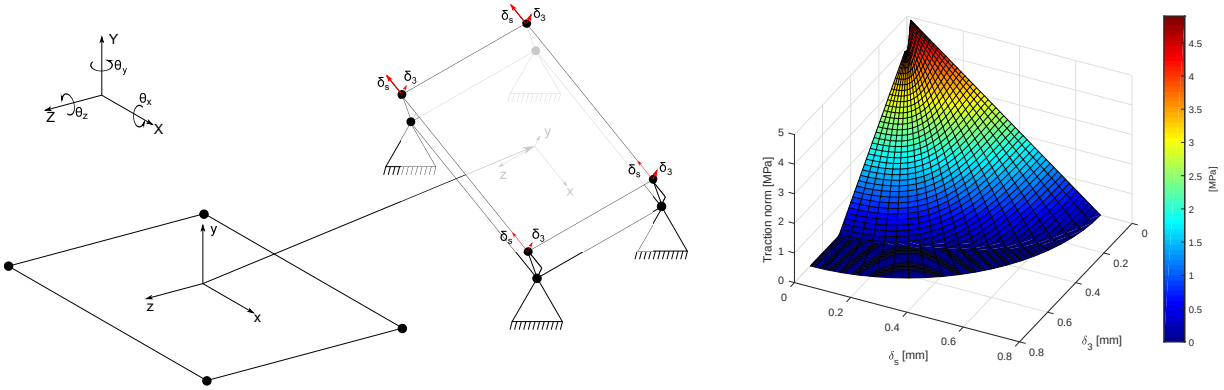

Figure 4: (Left) Sketch of the one element model along with the element and global coordinate systems. (Right) The simulated relation between the shear separation δ_s, positive normal separation δ_3, and the traction norm μ using the implemented element.

3.2. Element behavior - Mode I

The effect of the adaptive integration scheme for the cohesive element is easily illustrated by considering a simple one element model loaded in pure mode I, see Fig. 5. The top and bottom surfaces of the element are considered rigid and thus resemble a linear element. The node pair 1 and 5 and node pair 4 and 8 are loaded symmetrically with an increasing mode I opening displacement, $\Delta = \delta_I^{(1,5)} = \delta_I^{(4,8)}$. The nodes 2, 6, 3, and 7 are hinged so that the cohesive stress at locations between these node pairs are always zero. For simplicity the cohesive properties stated in Tab. 2 have been applied with a bilinear mode I cohesive law and an element length of $L_e = 2$ mm.

Table 2: Cohesive interface properties of the single element model used in the study of the implemented adaptive integration scheme.

$G_{Ic} = 0.5$ N/mm	$\tau_{Io} = 10$ MPa	$K = 10^7$ N/mm^3	$\delta_{Ic} = 0.1$ mm	$\delta_{Io} = 10^{-6}$ mm	$L_e = 2$ mm

An analytical solution to the problem has been formulated and solved in Maple [22] . The analytical solution for the reaction force per unit width, $\overline{R}$, of the element at the edge having the prescribed displacement, Δ, is given as

$$\overline{R} = \frac{\Delta K L_e}{3} \qquad \forall \quad \Delta \in]-\infty, \delta_{Io}] \quad \text{case 1} \tag{13}$$

$$\overline{R} = \frac{\delta_{Io} K L_e (\delta_{Ic}\delta_{Io}^2 + 2\Delta^3 - 3\delta_{Ic}\Delta^2)}{6\Delta^2(\delta_{Io} - \delta_{Ic})} \qquad \forall \quad \Delta \in [\delta_{Io}, \delta_{Ic}] \quad \text{case 2} \tag{14}$$

$$\overline{R} = \frac{\delta_{Io}\delta_{Ic} K L_e (\delta_{Io} + \delta_{Ic})}{6\Delta^2} \qquad \forall \quad \Delta \in [\delta_{Ic}, +\infty[\quad \text{case 3} \tag{15}$$

and reflect the three opening cases depicted in Fig. 5 which involves different states of damage within the cohesive element.

In Fig. 6, the analytical solution for the reaction force per unit width, $\overline{R}$, is shown as a function of the applied opening displacement together with numerical solutions of the one element model having different quadrature rules. In the legend the abbreviations NC and GL stand for Newton-Cotes quadrature and Gauss-Legendre quadrature, respectively. The number is the number of integration points along each element in-plane coordinate.

All integration schemes predict the peak load quite accurately. However, the dissipated energy per unit width, given by the area under the curve, depends significantly on the quadrature rule. Especially the 2 point Newton-Cotes

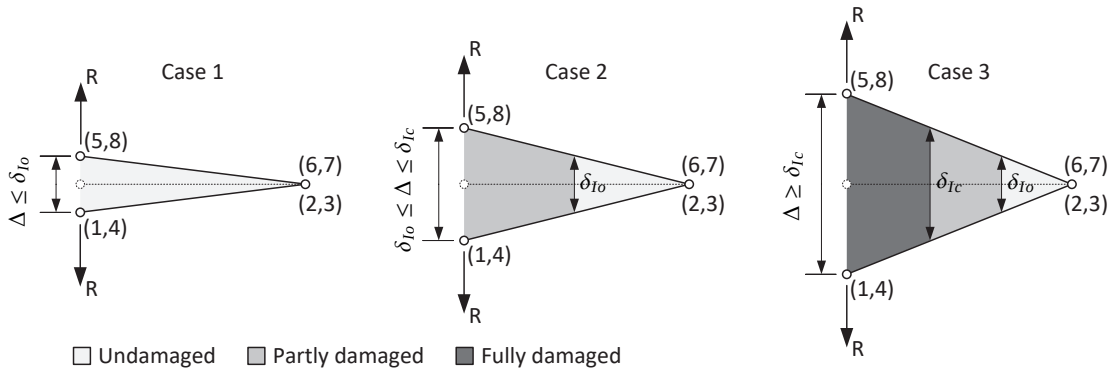

Figure 5: Illustration of the three damage cases for the analytical solution of the one element model subjected to pure mode I loading having a bilinear cohesize law.

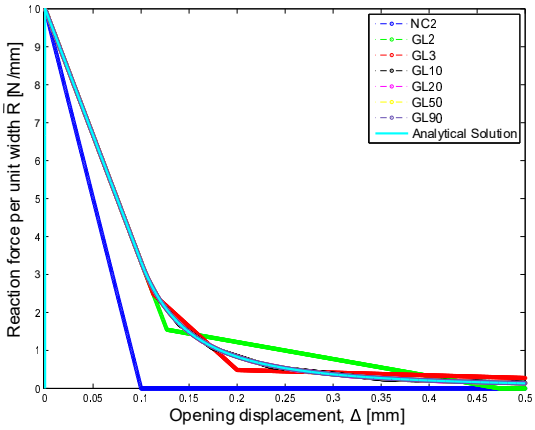

Figure 6: Reaction force per unit width along the element edge between node 1 and 4. The analytical solution is obtained with an element formulation in Maple. The other curves are finite element solutions using different integration schemes. Note that the curves GL10-GL90 in the graph are coincident with the analytical solution.

quadrature rule under predicts the energy dissipation by about 45%. The reason is due to premature failure when the nodal integration points obtain full damage when reaching a prescribed displacement of $\delta_{Ic} = 0.1mm$ and thus assume zero tractions throughout the element. In general the Gauss-Legendre quadrature rule performs better and more accurately captures the dissipated energy. With a 10 point Gauss-Legendre quadrature rule an almost exact solution is obtained with an error in dissipated energy below 0.5%. For this reason it is recommended to use at least a 10 point Gauss-Legendre quadrature rule within the adaptive integration scheme for the partly damaged elements in the process zone. Remark, that similar attempts to derive analytical formulas for a single element model have been done in [23] for a 4-noded 2D element. However, there seems to be a misprint or error in the formulas reported in [23] since the printed equations result in a discontinuous force-displacement curve.

3.3. Comparison with ANSYS INTER205

The following simulation results of a mixed-mode bending specimen serves to demonstrate that the element has an improved convergence rate and ability to converge compared to ANSYS element INTER205 which has the same element topology. INTER205 is based on the mixed mode constitutive law described in [13] which also uses a bilinear law in the pure crack loading modes. The mixed-mode bending specimen model is simulated by applying the boundary conditions similar to the mixed-mode bending apparatus [24], see Fig. 7, with the dimensions and material

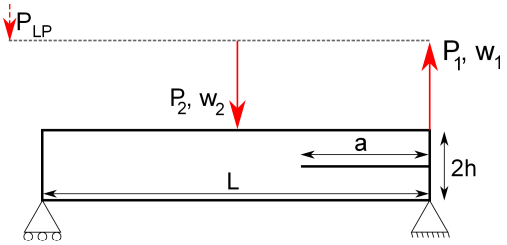

Figure 7: Finite element model of the mixed mode bending specimen.

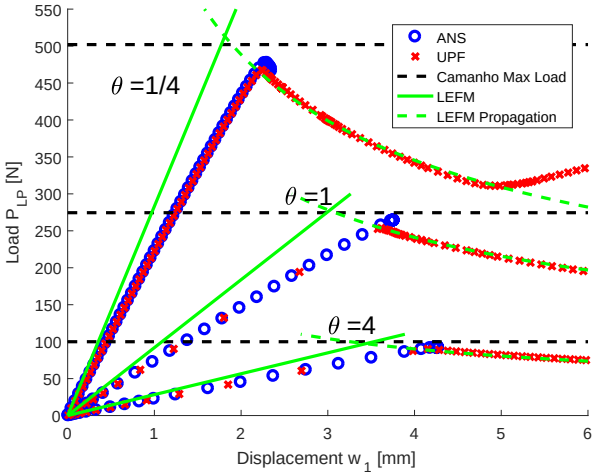

Figure 8: Simulation results of the MMB specimen. ANS: ANSYS INTER205 element. UPF: User programmed element. LEFM: Analytical solutions. Camanho Max Load: Max loads as found in [14].

data reported in Tab. 3. The mixed-mode bending specimen is considered in three different mode mixities $\theta = G_I/G_{II}$ = 1/4, 1, and 4 as defined in [14]. The dotted line in the model is a rigid load transferring element.

E_{11} 122.7 GPa	$E_{22} = E_{33}$ 10.1 GPa	$G_{12} = G_{13}$ 5.5 GPa	G_{23} 3.7 GPa	$\nu_{12} = \nu_{13}$ 0.25
ν_{23} 0.45	G_{Ic} 0.969 N/mm	G_{IIc} 1.717 N/mm	τ_{Io} 80 MPa	τ_{IIo} 100 MPa
L 102 mm	h 1.56 mm	t 25.4 mm	K 10^7 N/mm^3	

Table 3: Material data and dimensions for the mixed-mode bending specimen are taken from [14] and are for 24-ply unidirectional AS4/PEEK (APC2) carbon fibre reinforced composite specimens. Please note that the cohesize zone material properties not have been adjusted as suggested in [25].

The FEA models using either the developed UPF element formulation or the ANSYS INTER205 (ANS) element, respectively, use the same model setup, mesh size, and solution settings. The continuum of the mixed-mode bending specimen is discretized with the 3D 8-noded ANSYS SOLID185 element using the enhanced strain formulation having 1000 elements along the length, 1 element in the thickness, and 4 elements in the height of the specimen. The element length of the cohesize elements is 0.128mm which resulted in 10 elements in the cohesive zone for mode-mixity $\theta = 4$, 15-17 elements in the cohesive zone for mode-mixity $\theta = 1$, and 22 elements in the cohesive zone for mode-mixity $\theta = 1/4$. The standard Newton-Raphson solution procedure with displacement control with defaults settings and automatic time stepping has been applied. The maximum number of cumulative iterations until convergence failure is set to 800. The results using the developed UPF element are shown in Fig. 8 and compared to results using ANSYS INTER205 (ANS), Bernoulli-Euler beam based LEFM solutions, and the maximum load predictions of [14].

The solutions from the UPF and ANS element in Fig. 8 for the initial linear part of the curves are almost identical for all mode-mixities. Both solutions are more compliant than the LEFM solutions which are expected due to the used assumption of rigid boundary conditions of the Bernoulli-Euler based LEFM solutions. The load for unstable crack growth, see Tab. 4, predicted by the UPF and ANS element formulation are slightly different which might be due to different mixed-mode interaction criterion employed in the formulations. From Fig. 8 it may also be noted that the ANSYS INTER205 element formulation could not converge in the unstable propagation part for the different mixed-

Table 4: Number of iterations used in the simulations until the maximum load and the predicted maximum load at which unstable crack propagation occurs for three different mode mixities $\theta = G_I/G_{II} = 1/4$, 1, and 4. The abbreviation FTC stands for failed to converge in the entire solution range.

	$\theta = G_I/G_{II} = 1/4$		$\theta = G_I/G_{II} = 1$		$\theta = G_I/G_{II} = 4$	
Method	Load [N]	Iterations	Load [N]	Iterations	Load [N]	Iterations
ANS	477.4	248 (FTC)	264.0	194 (FTC)	92.2	420 (FTC)
UPF	467.5	82	254.0	101	90.1	134
LEFM	513.5	-	277.5	-	97.3	-
Experimental [14]	518.7	-	275.4	-	108.1	-

mode configurations. Reaching the maximum load the Newton-Raphson procedure initiated successive cut-backs until the maximum cumulative iteration number was reached. The UPF element formulation could obtain convergent solutions in the entire solution range. In Tab. 4 the number of equilibrium iterations in the Newton-Raphson procedure until reaching the maximum load is reported and it may be noted that the UPF element converges with much fewer iterations compared to the ANSYS INTER205 element. The UPF element converges to the maximum load using 48% – 68% fewer iterations compared to the ANSYS INTER205 element for identical standard solution settings.

4. Study on onset traction

It is well-known that in order to obtain convergent solutions using cohesize zone elements requires a relatively fine mesh. Typical recommendations suggest that the damage zone is discretized with a minimum of 3-10 elements, see [26]. A typical remedy to obtain convergent solutions using coarser meshes is to artificially increase the length of the damage zone by lowering the onset traction in the bilinear cohesive law keeping the critical energy release rate fixed [26, 27]. In effect the finite element model may be discretized using larger elements and yet provide convergent solutions and effectively reduce simulation time.

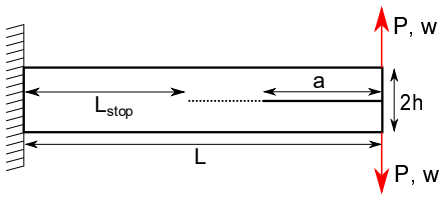

Figure 9: Finite element model of the DCB specimen.

In the following the approach of lowering the onset traction is investigated for different configurations of a DCB specimen in order to provide new insight into the approach and outline recommendations of practical usage. Material and geometric properties of the DCB specimens studied are based on [14] and are identical to those stated in Tab. 3. The DCB model, see Fig. 9, is discretized with the ANSYS SOLID185 element having 1000 elements along the length, 1 element in the thickness and 2 elements along the height of each DCB arm. The numerical simulation is conducted using the arc-length solver in ANSYS and the simulation is set to automatically stop when the crack has grown a certain distance such that the crack tip lies in a distance L_{stop} from the clamped end, see Fig. 9. The crack tip is defined as the point at which the normal opening displacement reaches δ_{Ic} and thus provides full damage. The DCB model is solved for different values of the onset traction as well as the initial crack length.

In Fig. 10 and 11, force-displacement simulation results of the DCB model with varying values of onset traction are shown for an initial crack length of 32.9 mm and 0.1 mm, respectively. In the crack propagation part (region with negative slope) all curves are coincident meaning that the global response is identical here. In the beginning and in the end of the curves differences are apparent. In general, for lower values of onset traction the load for unstable crack growth (peak load) is reduced and occurring at larger displacement. This is especially pronounced for the DCB model with an initial short crack of 0.1 mm, cf. Fig. 11. The endpoints of the force-displacement curves are connected to origo to make the endpoints visible. By inspecting the endpoints it is observed that the crack reaches its final length at

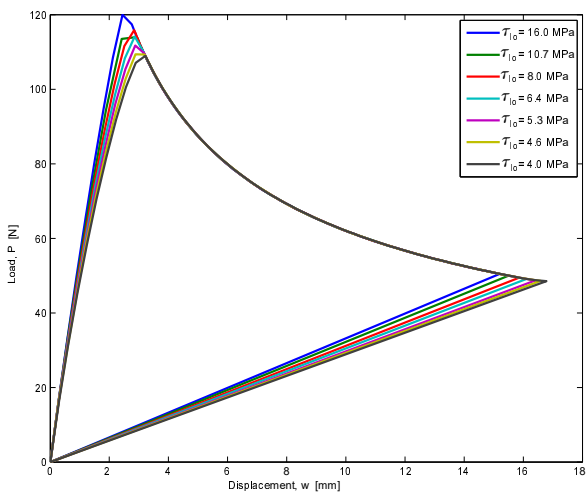

Figure 10: Force-displacement simulation results of DCB model with initial crack length of 32.9 mm with different values of onset traction. Stop criterion for the analysis set to $L_{stop} = L/7$.

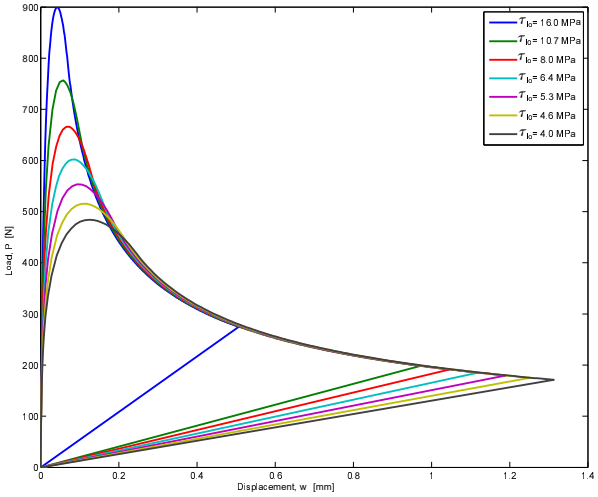

Figure 11: Force-displacement simulation results of DCB model with initial crack length of 0.1 mm with different values of onset traction. Stop criterion for the analysis set to $L_{stop} = L/1.2$.

larger displacement, w, at lower values of onset traction. Thus, lowering the onset traction provides more compliant response due to longer cohesive zones, whereas the value of onset traction is less important w.r.t. crack propagation.

To draw further conclusions from the results in Fig. 10 and 11 a numerical experiment is conducted in which the load for unstable crack growth is recorded for different combinations of initial crack length and onset traction. The results from this parametric study are shown in Fig. 12 and concludes that the load for unstable crack growth is very sensitive to the onset traction for short initial cracks whereas it is practically independent for large crack lengths. The reason for this is due to different relative interaction with the structural response, i.e. lower onset traction will produce longer cohesive zones and thus increase the compliance of the interface resulting in an apparent longer crack length. For short initial cracks this slight decrease in compliance of the interface, which is equivalent to a slight increase in crack length, will have strong structural interaction whereas it for relatively long cracks has no impact.

Thus, the study concludes that care must be taken if the approach of lowering the onset traction for obtaining convergent solutions in relatively coarse meshes is followed in cases where crack initiation or crack propagation of relative small cracks is to be examined using cohesive zone elements.

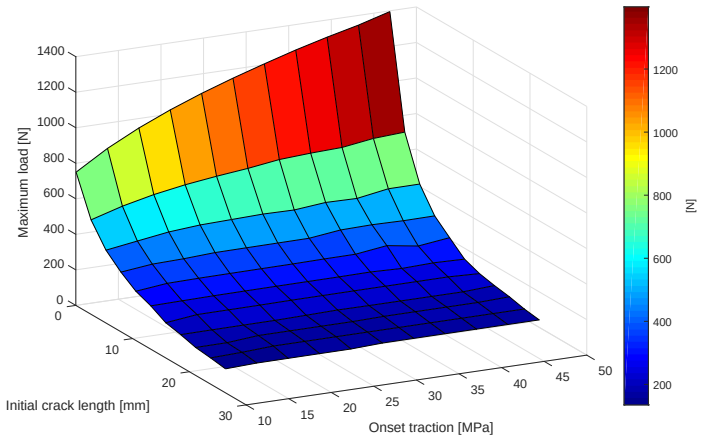

Figure 12: Predicted maximum load for unstable crack growth as function of initial crack length and onset traction of a DCB specimen.

5. Conclusion

A state-of-the-art cohesive zone finite element has been formulated and implemented in ANSYS Mechanical as a user programmable feature. The cohesive zone finite element is an 8-noded zero thickness brick element having a mixed-mode bilinear constitutive law defined by the modified BK-criterion and an adaptive numerical integration scheme is applied for improved accuracy and convergence behaviour of the elements. Additionally, non-standard post-processing options have been defined and implemented to precisely analyse the type and amount of delamination during simulation. The developed finite element has been verified on several examples and proves superior compared to the commercially available cohesive zone finite element INTER205 in ANSYS.

The typical remedy to obtain convergent solutions having coarser meshes is to artificially increase the length of the damage process zone by lowering the onset traction. A detailed study on DCB specimens showed that this approach may severely change the structural response and thus the maximum load for unstable crack growth. It was found that the effect on the structural response severely depends on the length of the initial crack. Thus special care must be taken and the authors do not recommend to use the approach for studies of crack initiation or crack propagation of relatively short cracks.

The presented cohesive finite element implementation in ANSYS Mechanical provides a framework for further research and development of cohesive zone models as well as making additional state-of-the-art simulation capabilities readily accessible.

Acknowledgements

The work was supported by the Danish Centre for Composite Structures and Materials for Wind Turbines (DCCSM), grant no. 09-067212 from the Danish Strategic Research Council. This support is gratefully acknowledged.

References

[1] A. A. Griffith, The phenomena of rupture and flow in solids, Philosophical Transactions of the Royal Society of London. Series A, Containing Papers of a Mathematical or Physical Character 221.
[2] G. R. Irwin, Analysis of stresses and strains near the end of a crack traversing a plate, Journal of Applied Mechanics 24 (1957) 361–364.
[3] G. I. Barenblatt, Concerning equilibrium cracks forming during brittle fracture: the stability of isolated cracks, Journal of Applied Mathematics and Mechanics 23 (1959) 622–636.
[4] D. S. Dugdale, Yielding of steel sheets containing slits, Journal of the Mechanics and Physics of Solids 8 (2) (1960) 100–104.
[5] A. Hillerborg, M. Modéer, P. E. Petersson, Analysis of crack formation and crack growth in concrete by means of fracture mechanics and finite elements, Cement and Concrete Research 6 (6) (1976) 773–781.
[6] A. Needleman, A continuum model for void nucleation by inclusion debonding, Journal of Applied Mechanics 54 (3) (1987) 525–531.

[7] G. Beer, An isoparametric joint/interface element for finite element analysis, International Journal for Numerical Methods in Engineering 21 (4) (1985) 585–600.
[8] A. Gens, I. Carol, E. Alonso, An interface element formulation for the analysis of soil-reinforcement interaction, Computers and Geotechnics 7 (1-2) (1989) 133–151.
[9] H. Schellekens, R. Borst, Geometrically and physically non-linear interface elements in finite element analysis of layered composite structures, in: J. Füller, G. Grüninger, K. Schulte, A. R. Bunsell, A. Massiah (Eds.), Developments in the Science and Technology of Composite Materials, Springer Netherlands, 1990, pp. 749–754.
[10] M. Ortiz, A. Pandolfi, Finite-deformation irreversible cohesive elements for three-dimensional crack-propagation analysis, International Journal for Numerical Methods in Engineering 44 (9) (1999) 1267–1282.
[11] A. de Andrés, J. L. Pérez, M. Ortiz, Elastoplastic finite element analysis of three-dimensional fatigue crack growth in aluminum shafts subjected to axial loading, International Journal of Solids and Structures 36 (15) (1999) 2231–2258.
[12] S. R. Chowdhury, R. Narasimhan, A cohesive finite element formulation for modelling fracture and delamination in solids, Sadhana Academy Proceedings in Engineering Sciences 25 (2000) 561–587.
[13] G. Alfano, M. A. Crisfield, Finite element interface models for the delamination analysis of laminated composites: mechanical and computational issues, International Journal for Numerical Methods in Engineering 50 (7) (2001) 1701–1736.
[14] P. P. Camanho, C. G. Davila, M. F. de Moura, Numerical simulation of mixed-mode progressive delamination in composite materials, Journal of Composite Materials 37 (16) (2003) 1415–1438.
[15] A. Turon, P. P. Camanho, J. Costa, C. G. Dávila, A damage model for the simulation of delamination in advanced composites under variable-mode loading, Mechanics of Materials 38 (11) (2006) 1072–1089.
[16] B. L. V. Bak, E. Lindgaard, E. Lund, Analysis of the integration of cohesive elements in regard to utilization of coarse mesh in laminated composite materials, International Journal for Numerical Methods in Engineering 99 (8) (2014) 566–586.
[17] ANSYS Inc., ANSYS Mechanical APDL Theory Reference ver. 17.2 (2016).
[18] B. L. V. Bak, A. Turon, E. Lindgaard, E. Lund, A Simulation Method for High-Cycle Fatigue-Driven Delamination using a Cohesive Zone Model, International Journal for Numerical Methods in Engineering 106 (2016) 163–191.
[19] M. L. Benzeggagh, M. Kenane, Measurement of mixed-mode delamination fracture toughness of unidirectional glass/epoxy composites with mixed-mode bending apparatus, Composites Science and Technology 56 (4) (1996) 439–449.
[20] Intel Corporation, Intel® Visual Fortran Compiler XE 12.1 Documentation (2011).
[21] MathWorks Inc., MATLAB Documentation R2016b (2016).
[22] Maplesoft, Maple User Manual ver. 17.0 (2013).
[23] B. C. Do, W. Liu, Q. D. Yang, X. Y. Su, Improved cohesive stress integration schemes for cohesive zone elements, Engineering Fracture Mechanics 107 (2013) 14–28. doi:10.1016/j.engfracmech.2013.04.009.
[24] ASTM D6671/D6671M-13e1, Standard Test Method for Mixed Mode I-Mode II Interlaminar Fracture Toughness of Unidirectional Fiber Reinforced Polymer Matrix Composites, Tech. rep., ASTM International, www.astm.org (2003).
[25] A. Turon, P. P. Camanho, J. Costa, J. Renart, Accurate simulation of delamination growth under mixed-mode loading using cohesive elements: Definition of interlaminar strengths and elastic stiffness, Composite Structures 92 (8) (2010) 1857–1864.
[26] A. Turon, C. Davila, P. Camanho, J. Costa, An engineering solution for mesh size effects in the simulation of delamination using cohesive zone models, Engineering Fracture Mechanics 74 (10) (2007) 1665–1682.
[27] L. C. T. Overgaard, E. Lund, P. P. Camanho, A methodology for the structural analysis of composite wind turbine blades under geometric and material induced instabilities, Computers & Structures 88 (19-20) (2010) 1092–1109.